Design of a Hybrid Busbar Filter Combining a Transmission-Line Busbar Filter and a One-Turn Inductor for DC-Fed Three-Phase Motor Drive Systems

Fang Luo, *Member, IEEE*, Andrew Carson Baisden, Dushan Boroyevich, *Fellow, IEEE*,
Khai D. T. Ngo, *Senior Member, IEEE*, Shuo Wang, *Senior Member, IEEE*,
and Paolo Mattavelli, *Senior Member, IEEE*

***Abstract*—The transmission-line busbar filter is an innovative high-density electromagnetic interference (EMI) containment solution for power electronics systems. It uses the concept of the transmission-line EMI filter as a part of the power interconnection to eliminate the EMI noises in power converters. This paper presents a systematic study of the transmission-line busbar filter in a motor drive system, which includes its design, modeling, and improvement using a hybrid approach. The paper investigates the relationship between the busbar filter's in-circuit attenuation and its geometry, and then derives a general design guideline for the transmission-line busbar EMI filters. To improve the performance of the transmission-line busbar filter, the paper proposes a hybrid busbar filter combining a transmission-line busbar filter and a one-turn inductor. This improvement provides much higher attenuation than the traditional transmission-line busbar filters. These proposed concepts have been verified experimentally not only with small-signal measurement but also with in-circuit tests in a medium-power motor drive system.**

***Index Terms*—Impedance mismatching, one-turn inductor, transmission-line electromagnetic interference (EMI) filter.**

I. INTRODUCTION

RESEARCH and development on all-electric transportation systems, such as all-electric airplane, all-electric ship and all-electric vehicles, become an important trend for the new generation of transportation systems. Increasing number of on-board power converters introduces more electromagnetic interference (EMI) between each other, and thus lots of bulky filters are needed to control the EMI between them. Passive filtering components engage a large proportion, in some cases as high as 1/3 [1], [2], of the converter's volume and weight. Integration technology can help to reduce the volume and weight of passive components by improving the form factor and/or by implementing multiple functions into one component [2]–[17]. Among the high-density filtering approaches, the transmission-line busbar filter provides an EMI containment solution to eliminate the conducted EMI noise using the power interconnects. This paper discusses the possibility and potential improvements of utilizing this idea for the motor drive systems in DC-fed all-electrical/more-electrical airplane applications.

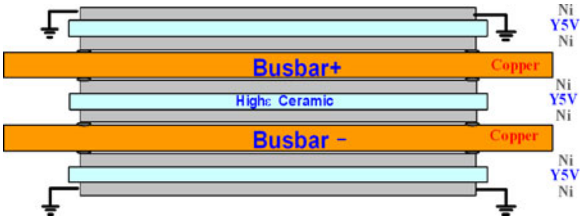

Fig. 1. Profile of the busbar filter.

The transmission-line EMI filter was proposed by the Rand Afrikaans University, Center for Power Electronics Systems at Virginia Tech, and McMaster University to attenuate high-frequency noise in power electronics systems, as stated in [3]. It is a low-loss/low-profile filter with good high-frequency performances. The transmission-line EMI filter has a planar low-profile structure without multioverlapped windings. This structure provides low parasitics, such as the equivalent parallel capacitor (EPC) of the inductor and the equivalent series inductor (ESL) of the capacitor. The manufacturing processes of this filter are compatible with the processes in the semiconductor industry, which provides the potential of low-cost mass production.

In a transmission-line EMI filter, different conductive paths are designed for the low-frequency power flow and the high-frequency noise current, respectively. It utilizes the transmission-line effects to attenuate high-frequency noises. Fig. 1 shows a cross-sectional view of a typical transmission-line EMI filter that contains both common-mode (CM) and differential-mode (DM) filtering elements. As shown in Fig. 1, in a transmission-line EMI filter, the low-frequency current mainly

---

Manuscript received June 5, 2012; revised September 12, 2012 and November 24, 2012; accepted January 19, 2013. Date of current version June 6, 2013. This work was supported by the ABB group and SAFRAN group. Recommended for publication by Associate Editor S. Wirasingha.

F. Luo, D. Boroyevich, K. D. T. Ngo, and P. Mattavelli are with the Center for Power Electronics Systems, Virginia Polytechnic Institute and State University, Blacksburg, VA 24061 USA (e-mail: fangluo@vt.edu; dushan@vt.edu; kdtn@vt.edu; mattavelli@ieee.org).

A. C. Baisden is with the Department of Space, Applied Physics Laboratory, Johns Hopkins University, Laurel, MD 20723 USA (e-mail: cbaisden@vt.edu).

S. Wang is with the Department of Electrical and Computer Engineering, University of Texas at San Antonio, San Antonio, TX 78249 USA (e-mail: shuowang@ieee.org).

Color versions of one or more of the figures in this paper are available online at http://ieeexplore.ieee.org.

Digital Object Identifier 10.1109/TPEL.2013.2244913

travels through the copper conductors, while the high-frequency current goes through the nickel conductors due to the skin effect and proximity effect. The nickel conductor is much more lossy than the copper conductor so that the noise current can be attenuated. The high-frequency ac loss in nickel layers includes eddy current loss and loss introduces by the fringing effect. Wolmarans *et al*. [4] determine that the ac loss is mainly contributed by eddy current loss; according to research works in [3], [5]–[9], [37], and finite element analysis (FEA) simulation in this paper, fringing effect can also be considered as the "mutual resistance" introduced by adjacent current flows. Both types of the ac loss are influenced by the nickel layer's thickness and its permeability, and both of them are frequency dependent [15]. The ac loss in the nickel layers provides damping to the noise current. The high-frequency noise current will be dissipated in the nickel layers. The high-frequency ac loss will generate some heat. However, the energy of ac noise is low so that the heat generated in nickel layers can be easily dissipated. This interesting idea has attracted a lot of attention. Wolmarans *et al*. [4]–[12] give a conceptual introduction to transmission-line EMI filters and their potential applications in power electronics systems. Liang *et al*. [14], [15] conducted a parametric study on the material properties and geometries impacts to the transmission-line EMI filter performance. Since the transmission-line EMI filter has a low-profile laminated structure with customizable shape, it can be made into different converter parts, such as a busbar (which makes a transmission-line busbar filter) or a planar power connector. van Wyk *et al*. [3], [4], [7], [8] proposed a low-pass interconnection for power electronics systems. However, the proposed concepts in these papers are mostly verified with the small-signal transfer gain test, and previous analysis on these filters mainly focused on the modeling and improvement of the transmission-line effects. It is not enough to provide the direct guidance for the transmission-line EMI filter's design and application in power electronics systems based on the previous knowledge. Moreover, it was proved that the EMI filter's in-circuit attention could be quite different from its small-signal test result [10].

Baisden *et al*. [10]–[12] reported some experimental results for the applications of a transmission-line busbar filter in a power factor correction (PFC) boost converter. They are early examples of the transmission-line busbar filter in-circuit verification. The test result in [11] and [12] showed that the busbar filter started to attenuate EMI noise at 400 kHz for CM and 200 kHz for DM. Fig. 1 illustrates the cross section of the transmission-line busbar filter described in [11] and [12]. In Fig. 1, nickel layers are sputtered and electroplated onto high-permittivity ceramic substrates. The nickel layers are bonded with the copper strips using conductive epoxy. The transmission-line busbar filter has been tested in a 400 W PFC circuit, and it has been proved that the filter can effectively attenuate the EMI noise [11], [12]. Baisden *et al*. [10], [12] investigated into the impedance interaction of the transmission-line busbar filter and the noise source/load, and then they gave the conclusion that the filter's low frequency (starts from 150 kHz to several megahertz) attenuation is not only determined by the filter's transfer gain, but also determined by the impedance mismatching between the filter and noise source: if the filter's output impedance is higher than the noise source impedance, appropriate attenuation can be achieved. However, Baisden *et al*. [11], [12] did not include a quantified analysis, nor gave more analysis on why and how does the impedance mismatching between the filter and the noise source can result in the required attenuation. Thus, previous references could not provide a simple and straightforward design model that links the transmission-line busbar filter and the required attenuation. It yet remains unclear that how to design the filter with proper impedance mismatching and attenuation requirement.

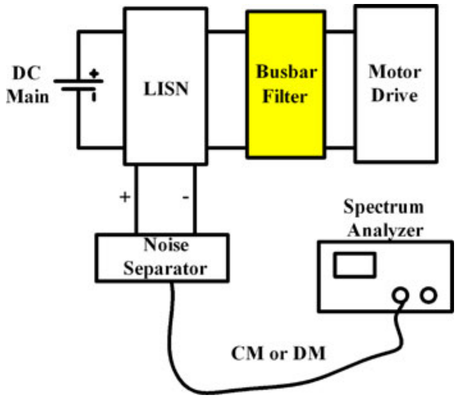

Fig. 2. Motor drive system EMI test.

Applying the transmission-line busbar filter described in [3]–[8] and [11] to a motor drive system introduces different problems [13]. The motor drive system has much lower switching frequencies, usually at tens of kilohertz, than the switching frequencies of the converters in [11] and [12]. This difference results in different EMI noise spectrums and may strongly degrade the busbar filter's performance [21]. The noise source and load impedances of the motor drive system are different from the PFC application in [10], so the transmission-line busbar filter's performance in the motor drive application remains unknown. Furthermore, the CM capacitance of the busbar filter in [10]–[12] can be as high as 1.1 μF, depending on different dimensions and materials. This CM capacitance value is usually limited (0.1 μF in [18]) in a real application by the standard. Besides, increasing dc input-side CM capacitance will increase the CM current on the ac output, and it will also increase the leakage current on the motor shaft and cause damage on the shaft [19]–[21]. Therefore, the filter's CM capacitance should be limited within a reasonable range.

The transmission-line busbar filter reported in previous literatures usually attenuates noises above hundreds of kilohertz, while typical EMI standards for motor drive systems, such as MIL-461, define the EMI measurement range from 10 kHz to 10 MHz. It is important and meaningful to develop a technique to improve the transmission-line busbar filter's performance by decreasing its cutoff frequency and/or increasing its attenuation. In this paper, a 2-kW dc-fed three-phase motor drive system is used as a test system. This research targets the dc-fed more-electric transportation system; thus, MIL-461 standard will be applied. The test setup is shown in Figs. 2 and 3. Fig. 4 illustrates the line impedance stabilization network (LISN) defined in

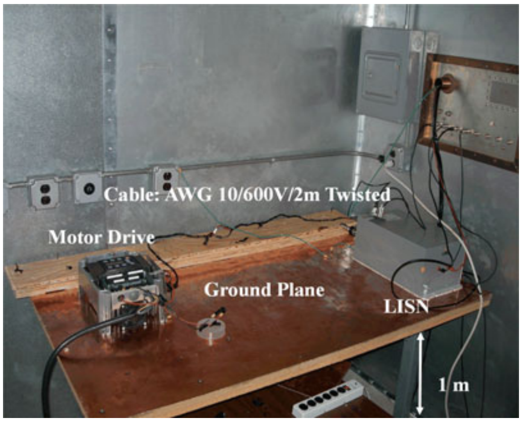

Fig. 3. Motor drive EMI test setup in an EMI test chamber.

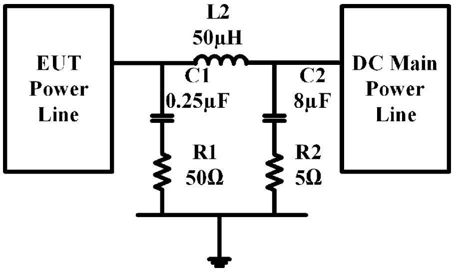

Fig. 4. LISN defined by MIL-461(one line).

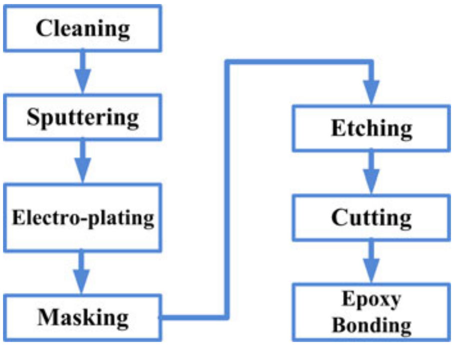

Fig. 5. Process of busbar filter fabrication.

MIL-461. The experiment is set up in a shielded EMI chamber according to the MIL-461. The device under test (DUT) and LISNs are placed on a ground plane connected to the real ground. The ground plane is lifted up from the floor 1 m. DUT and LISN are connected using a 2-m twisted cable. MIL-461 limit is defined by noise voltage on the LISN terminals. LISN is supposed to provide stable 50-Ω output impedance for all EMI test range (from 10 kHz to 10 MHz). However, according to the real LISN impedance defined in MIL-461, the real LISN impedance is lower than 50 Ω at low frequencies (from 10 kHz to 1 MHz). Hence, the noise measured at these frequencies is already attenuated by LISN. To separate CM and DM noises for filter design purpose, a noise separator [23]–[25] is needed in the test.

This paper introduces a series of research work of applying the transmission-line busbar filter concept and its improved solutions to motor drive systems for EMI noise reduction. It develops a simple design model and a guideline for the transmission-line busbar filter's application in power electronics systems. In this section, an overview of the transmission-line busbar filter and its history is given. Section II summarizes the filter fabrication processes. In Section III, the basic principle of transmission-line busbar filters is presented, and then the discussion on modeling and design of the busbar filter is given. In this section, a simple lumped model to correlate the filter's attenuation and its geometry is established. The impedance mismatching between the filter and noise propagation path is also included in the model, which determines the filter's in-circuit attenuation. Based on this knowledge, in Section IV, an improved busbar filter is proposed which combines transmission-line busbar filter and one-turn inductor concepts. Section V includes all the experimental results in both small-signal tests and in-circuit tests in a motor drive system. The proposed model and improved design are verified in a 2-kW motor drive system.

II. Fabrication Process of a Busbar Filter

As stated in Section I, a transmission-line busbar filter has a sandwich structure. It is a lamination of nickel layers, copper layers, and ceramic layers. The nickel layers are directly deposited onto the ceramic and bonded with copper conductors using silver epoxy.

The fabrication process of the transmission-line busbar filter is mostly compatible with the process in the semiconductor manufacturing. The bare ceramic substrate is first cleaned and then sputtered with nickel deposition. The thickness of sputtered nickel deposit is about 300 nm. The sputtered ceramic is then electroplated with nickel to make the nickel coating thick enough. After metallization, the substrate is processed with photolithography. The designed busbar pattern is masked on the metalized ceramic using photoresist, and then the exposed metal part is etched using ferric chloride. The patterned areas are cut by laser and bonded with copper parts using silver-conducted epoxy. Copper conductors are laminated in the middle of ceramics, between DM and CM high-frequency paths, to carry the low-frequency/dc current. Coppers and nickels electrically contact each other. The fabrication processes are illustrated in Fig. 5. Table I summarizes the geometry, materials, and electrical parameters of a busbar filter. The bonding material is silver conducted-epoxy H20E from EPOXY TECHNOLOGY.

III. Design and Improvement of Busbar Filters

This section presents the principle of busbar filter and its design.

A. *Noise Propagation in a Busbar Filter*

As stated in Section I, the busbar filter is a frequency-selective filter. The low frequency/DC current flows through the copper conductors. The copper conductor is a low impedance/low-loss path for the main power current in motor drive systems. The high-frequency noise current flows through nickel layers

TABLE I
PARAMETERS IN BASELINE BUSBAR FILTER DESIGN

Parts	Length (l)	With (w)	Thickness	Material	Capacitance/ Inductance
DM ceramic (effective)	100 mm	10mm	300μm	Y5V ($BaTiO_3$)	1.1μF
DM ceramic surface coating	100mm	10mm	10-15μm	Nickel	40nH/72 mΩ
DM (busbar) conductor	100mm	10mm	150μm	Copper	50nH/1 mΩ
CM ceramic (effective)	100mm	10mm	300μm	Y5V	1.1μF x 2
CM ceramic surface coating	100mm	10mm	10-15μm	Nickel	40nH/72 mΩ
Bonding	10mm	10mm		H20E (EPO-TEK®)	5mΩ

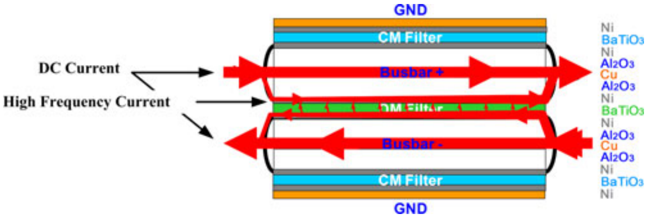

Fig. 6. DM current paths in a busbar filter.

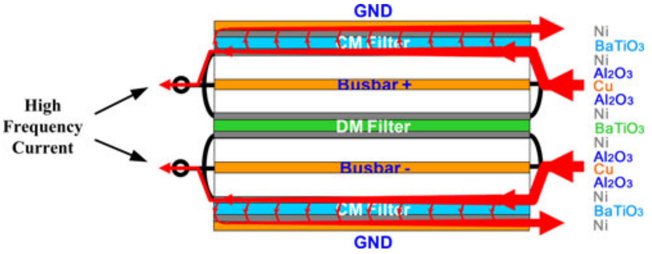

Fig. 7. CM current paths in a busbar filter.

instead of copper layers because of the skin effect and proximity effect. The dielectric layers ($BaTiO_3$) between adjacent nickel layers also create low impedance paths for the high-frequency noise current. Therefore, the high-frequency noise current is either shorted by the dielectric layers or attenuated by ac resistance in nickel layers. Fig. 6 illustrates the DM current paths. The same mechanism also holds for CM noise current filtering. As shown in Fig. 7, the high-frequency CM noise currents flow through the inner nickel layers due to the proximity effect and the skin effect. The high-frequency CM current is dissipated along the nickel layer and shorted by dielectric layers directly into the system ground. In the transmission-line busbar filter design proposed in [11], Al_2O_3 layers are added as a mechanical support to hold the ceramics. It does not contribute to the electrical characteristic of the filter. The transmission-line busbar filter designed in this paper has high enough mechanical strength, since the ceramics are bonded with thick copper together. Thus, the Al_2O_3 layers are removed. Fig. 8 shows the installation of the transmission-line busbar filter described in [11] and [12]. The filter is installed vertically, and the ground copper foils are symmetrically connected to the ground. This configuration ensures the balance of grounding impedances, and this configuration is thus used in the filter installation in the design presented in this paper. Baisden *et al*. [11], [12], [40] provide detail analyses on how the grounding will impact the filter's attenuation.

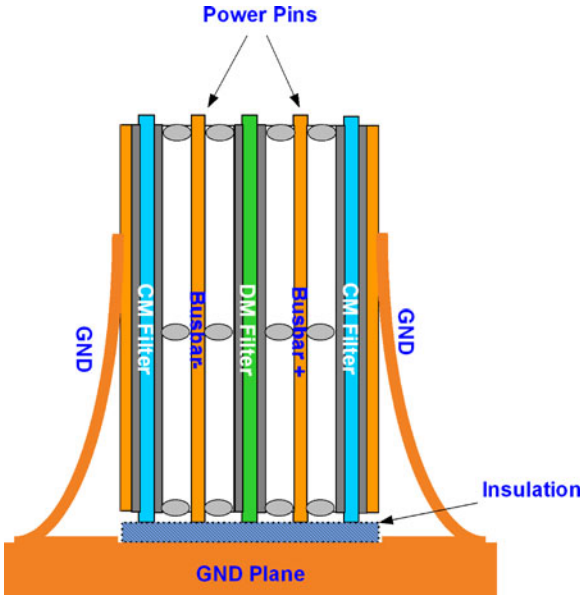

Fig. 8. Front view of the busbar filter with grounding connections.

B. Modeling and Design of Busbar Filters

There are different models, such as distributed models, quasi-distributed models, and lumped models, available to represent the performance of a transmission-line EMI filter. The distributed model and the quasi-distributed model use a group of cascaded cells to present the transmission line nature of the filter. These cells include inductance, resistance, capacitance, and conductance per section/distance. A common practice to determine the number of cells is to divide the transmission line length by its excitation wavelength if the excitation wavelength is no longer than the transmission-line filter's dimension along the propagation direction [26], [27]. The wavelength is calculated by $\lambda = c/f$ (where λ is the wavelength, c is the speed of light in the propagation media, and f is the frequency). In the free air, the noise wavelength is comparable to the busbar filter size (100 mm) only when the noise frequency is higher than 100 MHz. Thus, the lumped model works well for those low noise frequencies with long wavelength; when noise frequency exceeds 1 MHz (between 1 MHz and 10 MHz), considering the wave propagation in nickel layers, the high-frequency transmission-line effect starts influencing the wave propagation. However, it still does not enter the typical transmission-line effect yet; thus, the complex quasi-distributed/distributed model will not show too much difference compared to the lumped model. Based on these reasons, this paper proposed a lumped model for the frequency range 10 kHz–10 MHz with frequency-dependent parameters. This model provides both simplicity and acceptable accuracy for EMI noise reduction. In a motor drive application, the conducted EMI ranges from 10 kHz to 10 MHz, according to different EMI

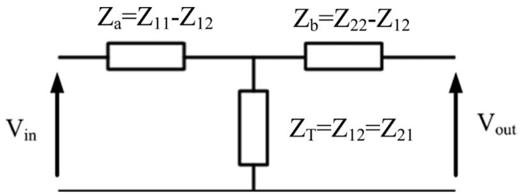

Fig. 9. "T" equivalent circuit of the transmission-line filter.

standards. This leads to relatively long wavelengths even in the transmission-line filters made with high permittivity and high permeability materials. Because of this, the transmission-line effect in the filter does not play an important role in the filter's attenuation below 1 MHz. In this case, a lumped model is enough to predict the performance of the transmission-line busbar filters in a wide frequency range with good accuracy; on the other hand, a distributed model works better above 1 MHz for the modeling of all the filter resonances at high frequencies, so it helps to explain some high-frequency phenomena. From the practical point of view, as long as the high-frequency noises can be suppressed below the standard's limit, the lumped model can be a satisfactory choice for the filter design

$$\begin{cases} Z_a = Z_b = Z_0 l k_1/2 \\ Z_a = Z_{11} - Z_{12} \\ Z_b = Z_{22} - Z_{12} \\ Z_{21} = Z_{12} = Y_0 l k_2 = Z_T \\ k_1 = k_2 = 1 (<100 \text{ MHz}) \\ Z_0 = \dfrac{Z_{\mathrm{Ni}}(f) \cdot Z_{\mathrm{Cu}}(f)}{Z_{\mathrm{Ni}}(f) + Z_{\mathrm{Cu}}(f)} \\ Y_0 = G_0(f) + j\omega C_0 \end{cases} \tag{1}$$

$$R(f) = \begin{cases} \dfrac{1}{\sigma w t} & \delta(f) > t \quad [\Omega/\mathrm{m}] \\ \dfrac{2}{\sigma w \delta(f)} & \delta(f) < t \quad [\Omega/\mathrm{m}] \end{cases} \tag{2}$$

$$L_{\mathrm{HF}}(f) = \frac{2}{3}\mu_0\mu_r \frac{\delta}{w} e^{1-\frac{t}{\delta}} \quad [\mathrm{H/m}] \tag{3}$$

$$L_{\mathrm{LF}} = \mu_0 \mu_r \frac{d}{w} \quad [\mathrm{H/m}] \tag{4}$$

$$L_{\mathrm{total}}(f) = L_{\mathrm{HF}}(f) + L_{\mathrm{LF}} \quad [\mathrm{H/m}] \tag{5}$$

$$Z_{\mathrm{Ni}}(f) = R_{\mathrm{N}i}(f) + j\omega L_{\mathrm{Ni\_total}}(f) \tag{6}$$

$$Z_{\mathrm{Cu}}(f) = R_{\mathrm{Cu}}(f) + j\omega L_{\mathrm{Cu\_total}}(f) \tag{7}$$

$$C_0 = \varepsilon_0 \varepsilon_r(v) \frac{w}{d} \quad [\mathrm{F/m}] \tag{8}$$

$$G_0(f) = j\omega C_0 \cdot \tan\delta \quad [\mathrm{S/m}] \tag{9}$$

Fig. 9 gives a typical representation of the transmission-line busbar filters using a lumped "T" structure, and the components in this structure are represented by impedance parameters (Z-parameters) [27]. Parameters in Fig. 9 can be calculated using equation set (1) [4], [26], [27], which is an equation set from text book. Here, l is the length of the transmission-line filter, Z_0 represents the metal layer impedances, and Y_0 represents conductance of the dielectric layers. k_1 and k_2 are the coefficients representing transmission-line effects. Both of the coefficients are equal to 1 when the frequency is lower than 100 MHz. As stated previously, different current components flow through different paths in the transmission-line busbar filter. The nickel layers and copper conductors are bonded using the conductive epoxy, so different metal layers in the busbar filter can be modeled separately in Fig. 10. The total impedance Z_0 can be calculated as the paralleled impedances from nickel layer and copper layer [4] Fig. 11 and Fig. 12, respectively, illustrate the DM and CM equivalent circuits of the busbar filter according to the structure shown in Fig.10.

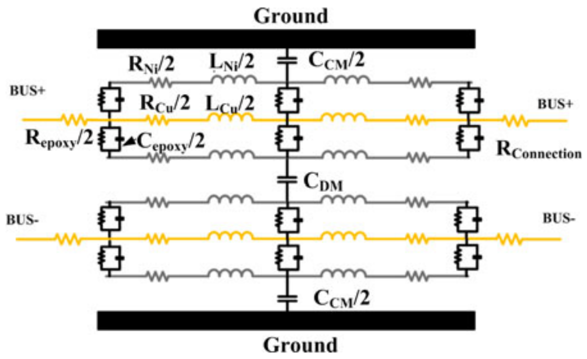

Fig. 10. Equivalent circuit for a busbar filter.

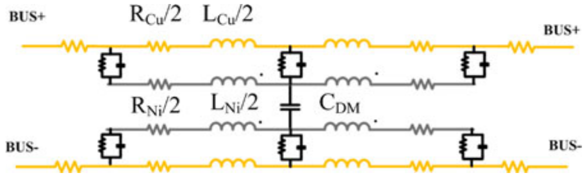

Fig. 11. DM equivalent circuit.

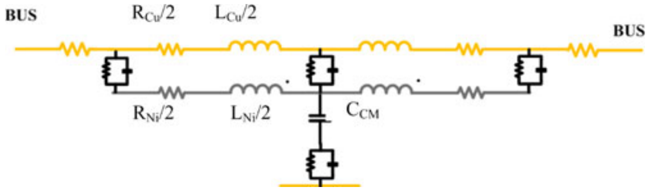

Fig. 12. CM equivalent circuit (for one side).

Equation (2) gives the ac resistance calculation for different metal layers [4], [26], where t is the thickness of the metal, w is the width of the conductor, σ is the conductivity of the material, and δ stands for the skin depth of the metal at different frequencies. The inductance of the conductor loop also contains high-frequency inductance and low-frequency inductance. Equation (3) gives the expression for high-frequency loop inductance including skin effect. Equation (4) gives the low-frequency loop inductance using a microstrip model. In (4), d represents the distance between two conductors, usually it is dominated by the thickness of the dielectric layer. Equations (5)–(7) can be used to calculate the metal layer impedances [4], [14], [15]. The capacitance of BaT$_{\mathrm{i}}$O$_3$ Ceramic (Y5V) layers in the busbar filter can be evaluated using the filter's geometry and the thickness of the dielectric layer, as shown in (8). When applying the busbar filter to motor drive systems, the permittivity of ceramic drops with dc voltage bias; therefore, the filter's capacitance also decreases. Liang *et al.* [14] investigated the impacts from dc bias voltage on the capacitance. In the applications described in this paper, the DM voltage is 300 V, and the CM DC bias is 150 V because the system is symmetrically grounded via balanced CM capacitors. The transmission-line busbar filter described in the last section has DM capacitance 0.2 μF and CM capacitance 0.5 μF, in this real application with dc voltage bias. Equation (9) is for conductance calculation. The loss factor tanδ is assumed to be a typical value of 0.01 [4]. Equations (2)–(9) come from the fundamental equations of skin effect; they give the basic support to calculate the filter's inductance, capacitance, resistance, and conductance. Wolmarans *et al.* [4] linked these basic equations to the geometry of the transmission-line busbar filter. It gives a more clear representation of relationship between the busbar filter parameters and its electrical characteristic. Based on the equivalent circuit and the parameters of the transmission-line busbar filter, the filter's voltage transfer gain (VTG) can be calculated using (10). The VTG represents the attenuation ratio between the filter's output voltage and input voltage, without the impacts from source/load impedances. It can be derived from equation set (1) and Fig. 9. Equation (10) shows the VTG of the transmission-line busbar filter for the specific geometry described in the last section. As shown in (10), the filter's VTG is only related to the conductor's width/thickness and the thickness dielectric material.

Here, in (1)–(9), d is the distance between two conductors (DM), or the distance between the conductors to the grounding connection (CM).

From Fig. 9, the voltage ratio between V_{out} and V_{in} can be presented by $\text{VTG} = \frac{V_{\text{out}}}{V_{\text{in}}} = \frac{Z_T}{Z_a}$ and substituting in $Z_T = Z_{12}, Z_a = Z_{11} - Z_{12}$, it can be written as

$$\text{VTG} = \frac{1}{\frac{Z_{11}}{Z_{12}} - 1}.$$

Substitute in $Z_T = Y_0 l k_2$, $Z_a = Z_0 l k_1 / 2$, it can also be written as

$$\text{VTG} = \frac{V_{\text{out}}}{V_{\text{in}}} = \frac{Z_T}{Z_a} = \frac{1}{\frac{Z_{11}}{Z_{12}} - 1} = 2 \cdot \frac{Y_0}{Z_0}. \qquad (10)$$

The filter's resistance, inductance, and capacitance can also be extracted using FEA simulation. ANSYS Maxwell 2-D/3-D eddy current simulation was used in this research, and the simulation geometry is exactly the same as described in previous sections. The current density in nickel layers increases as the excitation frequency increases, as illustrated in Fig. 13. It means the nickel layer has high ac resistance at high frequencies.

The permeability of the nickel layers in the transmission-line busbar filter varies in a wide frequency range due to the physical characteristics of electroplated nickel, which is different from the ideal nickel. Moreover, the permeability of magnetic materials decreases when its excitation frequency increases. This variation impacts the high-frequency inductance and resistance of the transmission-line busbar filter. Parametric study in FEA simulation can help to understand this impact. The ANSYS Maxwell simulation results in Figs. 14 and 15 illustrate the ac inductance (include both mutual inductance and self-inductance) and ac resistance (include both mutual resistance and self- resistance [37]) as a function of the nickel layer's permeability and the excitation frequency. Generally speaking, the ac inductance decreases as the excitation frequency increases, because the permeability drops as the frequency increases; on the other hand, the ac resistance increases as the frequency increases since the skin and proximity effects get stronger at higher frequencies. Both ac inductance and ac resistance decrease as the permeability drops, but their variations are negligible compared with the skin and proximity effects [15], [26], as shown in Figs. 14 and 15.

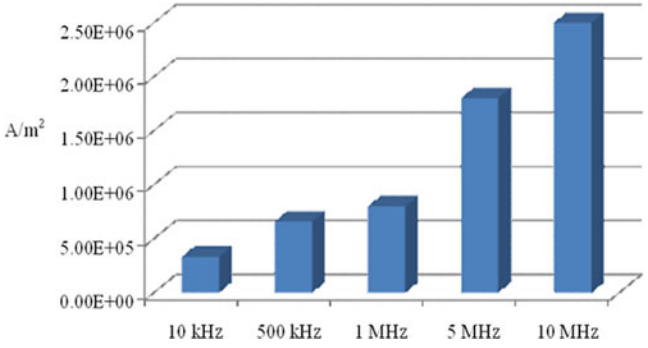

Fig. 13. Current density in nickel layers at different frequencies.

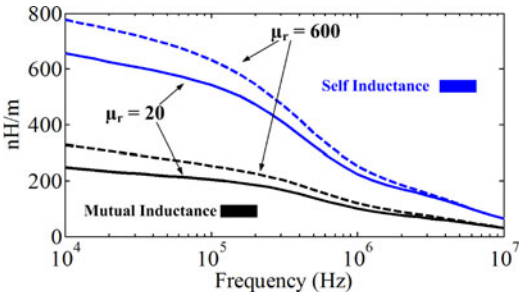

Fig. 14. Nickel permeability impacts on the inductance.

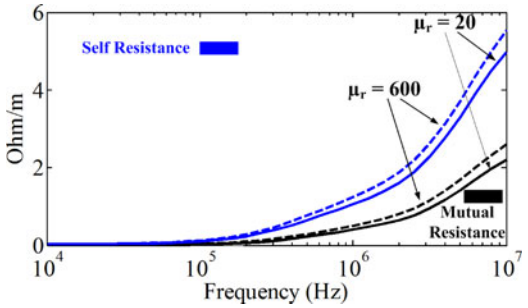

Fig. 15. Nickel permeability impacts on the resistance.

Fig. 16 illustrates the comparison of the filter's characteristic impedances extracted by FEA simulation and the analytical model. The FEA simulation and the analytical model in this paper match well below 1 MHz. However, the results deviate after 1 MHz. The analytical model used in this paper is a

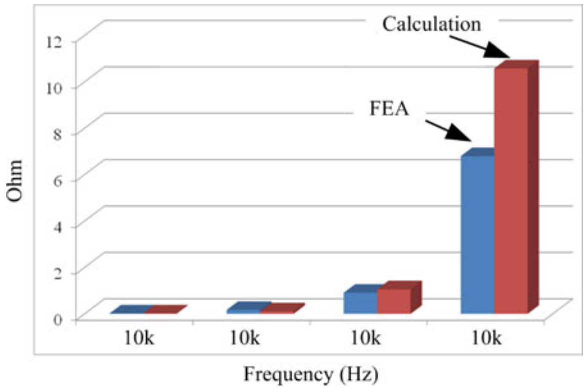

Fig. 16. Comparisons of the filter's characteristic impedances using FEA extraction and analytical model at different frequencies.

simplified model with low-frequency assumptions. The impedance introduced by the eddy current effect is simply added with the low-frequency impedances in this analytical model. FEA simulation gives more accurate solution since it includes the mutual coupling, the eddy current effect, and the fringing effect. Furthermore, FEA simulation can include the frequency-dependent properties of materials, which also significantly influence the characteristic of the filter.

C. Busbar Filter's In-Circuit Attenuation

The transmission-line busbar filter's VTG is supposed to represent the filter's attenuation. However, it cannot fully represent the filter's practical performances in different systems due to the interactions between the filter and the noise source/load impedances. The noise source/load impedances vary in different systems. The filter's in-circuit attenuation (in-circuit insertion gain) is defined as the noise ratio with the filter and without the filter. When the transmission-line busbar filter is applied in a motor drive system, its in-circuit attenuation cannot be simply represented with its VTG, because the in-circuit attenuation is strongly related to the noise source and load impedances. Fang *et al.* [22], [29]–[36] proposed equivalent models for the noise propagation paths of both CM and DM noises, and discussed the relationship between the filter's in-circuit attenuation and the impedance interactions . It is proved in these research works that the noise source and the noise propagation path can be modeled with the converter system's offline impedances. Therefore, the filter's in-circuit attenuation can be represented by V_o/V_s, as shown in Fig. 16. In Fig. 16, Z_s presents the sum of the noise source impedance and the parasitic impedances of propagation path. Z_{LISN} represents the input impedance of LISNs. V_N is the noise source voltage. V_s is the noise voltage measured on LISNs without the filter and V_o is the noise voltage measured on LISNs with the filter. When the transmission-line busbar filter is inserted to the system, the filter's input impedance/output impedances Z_{11} and Z_{22} interact with Z_s and Z_{LISN}, which determines the in-circuit attenuation of the filter, as shown in (11). Equation (11) also shows that filter's in-circuit attenuation is not only related to filter's impedances Z_0 and admittance Y_0 (these are the functions of the thickness and width of conductor/dielectric layers), but also related to the filter's length l.

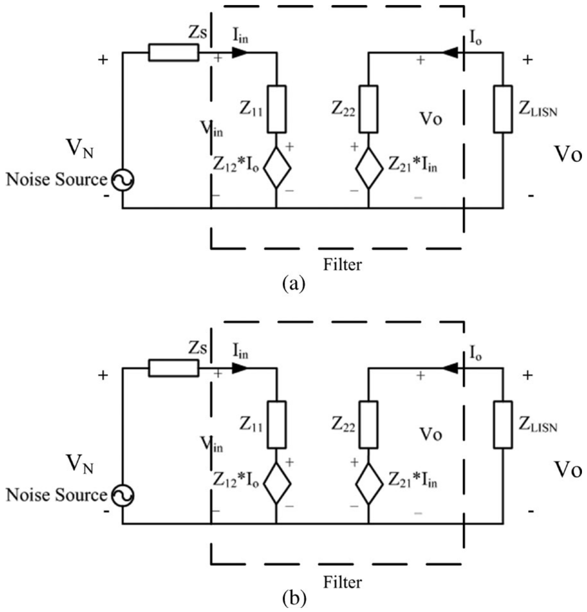

(a)

(b)

Fig. 17. EMI filter's in-circuit attenuation. (a) Equivalent circuit for a motor drive system without filter. (b) Equivalent circuit for a motor drive system with filter.

From Fig. 17(a), it can be found that

$$V_s = \frac{V_N Z_{\text{LISN}}}{(Z_{\text{LISN}} + Z_s)}.$$

Using Fig. 9 to present the filter topology, and defining // as the parallel of two impedances, it can be found that

$$V_o = \frac{V_N Z_{\text{LISN}}}{(Z_a + Z_s + Z_T//(Z_b + Z_{\text{LISN}}))} \cdot \frac{(Z_T//(Z_b + Z_{\text{LISN}}))}{(Z_b + Z_{\text{LISN}})}.$$

Substituting (1) in Fig. 17(b), we obtain V_o/V_s as

$$\begin{aligned}\frac{V_o}{V_s} &= \frac{(Z_{\text{LISN}} + Z_s)Z_T}{Z_{11}Z_{22} + Z_{11}Z_{\text{LISN}} + Z_{22}Z_s + Z_{\text{LISN}}Z_s - Z_T^2}\\ &= \frac{(Z_{\text{LISN}} + Z_s)Y_0 l}{((Z_0/2)^2 + Y_0 Z_0)l^2 + (Y_0 + Z_0/2)(Z_{\text{LISN}} + Z_s)l + Z_{\text{LISN}} \cdot Z_s}.\end{aligned} \tag{11}$$

IV. HYBRID BUSBAR FILTER WHICH COMBINES BUSBAR FILTER AND ONE-TURN INDUCTOR

As stated in Section I, the transmission-line busbar filter usually provides significant attenuation above hundreds of kilohertz. On the other hand, the EMI measurement frequency ranges from 10 kHz to 10 MHz. Campbell *et al.* [7] proposed a step-edge transmission line to increase the filter's stopband. However, it only works in megahertz range. According to (11), increasing Z_0, Y_0 and l can increase the filter's in-circuit attenuation with the same materials in design. It means to increase the filter's length or conductor's width, or to decrease the dielectric thickness, can help to improve the filter's performances. Increasing the filter's length is equivalent to increasing the metal layer inductance, while increasing the conductor's width or

TABLE II
ELECTRICAL PARAMETERS IN BASELINE BUSBAR FILTER DESIGN

Parts	Small Signal Value	In-circuit Value
DM capacitance	0.57μF	0.2μF
DM inductance	40nH	40nH
DM resistance	72mΩ	72mΩ
CM capacitance	1.1μF	0.5μF
CM inductance	40nH	40nH
CM resistance	72mΩ	72mΩ

decreasing the dielectric thickness is equivalent to increasing the capacitance.

Increasing the filter inductance or capacitance can both help to improve the filter's attenuation. In the DM filter, the switching load current will go through the DM inductor. High DM inductance leads to high transient energy storage in the DM inductor, and this energy will be transferred into the dc-link capacitor during switching intervals. Therefore, increasing DM inductance will increase the voltage stress on the dc link. It has been reported and analyzed in details that increasing DM inductance increases the voltage overshoot on the dc link [38]. Because of this influence, to improve the filter's DM performance, it would be preferable to increase DM capacitance by decreasing the dielectric layer thickness as long as there is no inrush-current issue or insulation issue. The minimum achievable dielectric thickness is limited by the availability of the material and its dielectric strength; in CM filters, the CM capacitance is limited by the leakage currents specified in standards [2], [18]. Because of this limit, increasing CM inductance is a more efficient way to improve the transmission-line busbar filter's CM performance. Increasing filter dimensions can also be a solution to increase inductances. However, the improvement is limited by the high power density requirement. An alternative way to increase the CM inductances without increasing the filter size is to use a magnetic core on the busbar filter, which is equivalent to adding a one-turn inductor to the busbar filter. With the help of magnetic cores, the busbar filter has high CM inductance and does not change the filter's geometry. One-turn inductor is very suitable for medium-/high-power applications since it is hard to make multiturn windings on a magnetic core with big conductors. The new busbar filter that combines the transmission-line busbar filter and the one-turn inductor is then called the "improved busbar filter (improved design)" or, the "hybrid busbar filter." And hereafter, the transmission-line busbar filter described in Section II is taken as the "baseline filter."

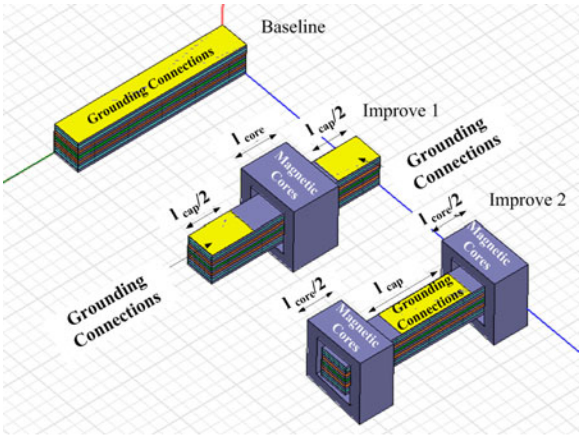

Fig. 18. Possible improved designs.

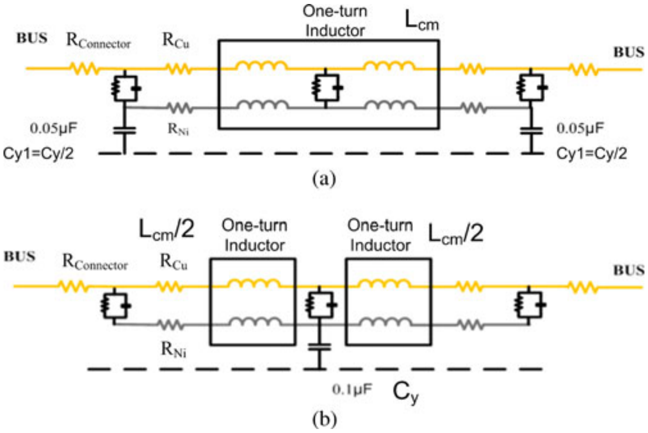

Fig. 19. Equivalent circuits of different configurations. (a) Equivalent circuit of Improved 1 design. (b) Equivalent circuit of Improved 2 design.

The previous design of the transmission-line busbar filter in Table II has a CM capacitance value of 0.5 μF. It is much higher than the safety limit. In the improved design, the CM capacitance is reduced to 0.1 μF to comply with the safety standards [2]. Compared to the previous transmission-line busbar filter, the filter with limited grounding capacitance has less CM capacitance value, so it is called the "reduced capacitance filter." Once the grounding capacitance is reduced, the filter's CM attenuation is reduced too. Clamping a magnetic core onto the busbar filter can effectively increase the CM inductance, and then increases its CM attenuation again. The ground layers of the busbar filter need to be removed inside the magnetic core; otherwise, the CM fluxes would be canceled. Due to the limited availability of ceramic material, the DM part of the improved busbar filter stays the same as described in previous sections. There are two configurations of the improved design with additional magnetic cores: one core is located in the middle (Improved 1) or two cores are located on two terminals (Improved 2), as shown in Fig. 17. The magnetic cores in the two proposed configurations have the same core cross area and same total core height. Improved designs 1 and 2 have the same total inductance and capacitance. Improved design 1 obtains one big inductor in the middle, equally splits the capacitors into two parts, and symmetrically places the capacitors on both sides of the inductor; improved design 2 obtains the grounding connecting in the middle, equally splits the inductor into two parts, and symmetrically places them on both ends of the filter. Fig. 18 illustrates the difference in the improved filters.

These two configurations result in two different equivalent circuits and different attenuation as shown in Fig. 19. Fig. 20

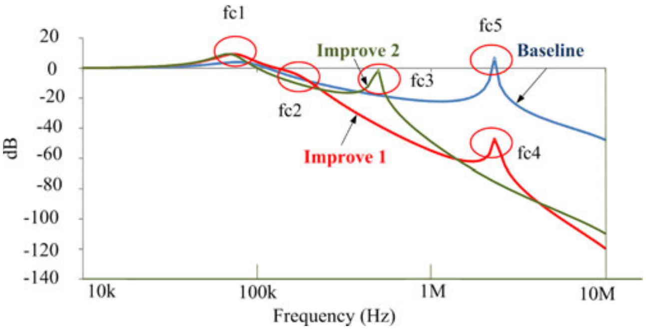

Fig. 20. Simulated in-circuit attenuation of different configurations.

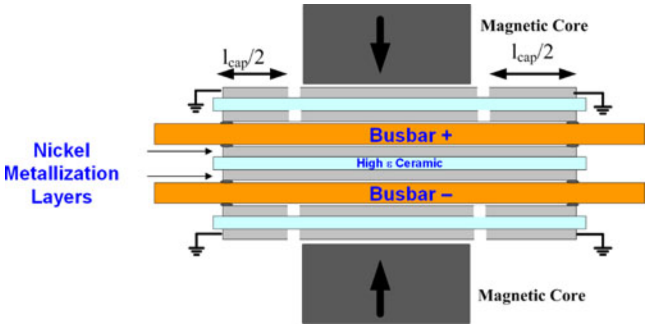

Fig. 21. Improved busbar filter design with one-turn inductor.

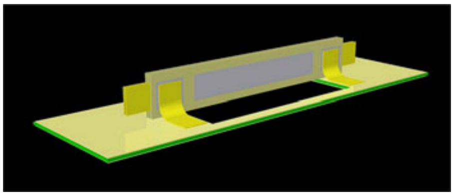

Fig. 22. Busbar filter with limited grounding capacitance (reduced capacitance filter).

shows the simulated real in-circuit attenuation of different busbar filters, including the baseline filter and two improved designs. The simulation shown in Fig. 20 includes the influences from the noise source/load impedances, but no ac resistance of the filter. In this simulation, the CM noise source impedance is represented by a small stray capacitor C_s in series with a stray inductor L_s, and the noise load impedance is considered to be the output impedance of the LISN (25 Ω for CM). The differences between filters come from two parts: the impedance interactions between the noise propagation path and filter impedances; and the filter's resonant.

The baseline filter has very low CM inductance. It can be considered to be a CM capacitor. The in-circuit attenuation comes from the impedance mismatching between the filter's CM capacitor and the LISN output impedance, and the resonant frequency is determined by the cutoff frequency of the RLISN and the CM capacitor. At the cutoff frequency, the impedance of CM capacitors is lower than the CM output impedance of the LISN (25 Ω), the filter starts bypassing the noise via the CM capacitor. At low frequencies, the baseline busbar filter performs like a first-order filter. The attenuation of baseline filter is −20 dB/dec. The resonance at 2.5 MHz is the resonant created by the noise source. Fang *et al.* [35], [36], [39], [40] give more detailed discussion on this phenomenon.

In improved designs 1 and 2, extra magnetic cores are added on the transmission-line busbar filter, and the resonant frequency is then determined by the inductance and capacitance values. Improved designs 1 and 2 have the same total inductance and capacitance. Improved design 1 obtains the big inductor in the middle, equally splits the capacitors into two parts, and symmetrically places the capacitors on both sides of the inductor; improved design 2 obtains the grounding connecting in the middle, equally splits the inductor into two parts, and symmetrically places them on both ends of the filter.

Improved design 1 can be seen as a *CLC* filter, since it has the one-turn inductor in the middle and grounding connections on both sides. In this case, the first cutoff frequency f_{c1} is determined by the total filter inductance L_{cm} and one of the capacitor $C_y/2$, and the filter provides −40 dB/dec attenuation. When the frequency keeps increasing, at f_{c2}, impedance of the grounding capacitor $C_y/2$ is lower than the LISN impedance, so that the noise is by passed by the C_y capacitor and the filter provides −60 dB/dec attenuation. The resonance at 2.5 MHz is also the resonant created by the noise source.

Improved design 2 can be seen as an *LCL* filter, since it obtains the grounding connecting in the middle, equally splits the inductor into two parts, and symmetrically places them on both ends of the filter. In this case, the first cutoff frequency f_{c1} is determined by the filter's total capacitance C_y and one of the filter inductor $L_{\mathrm{cm}}/2$, and the filter provides −40 dB/dec attenuation. When the frequency keeps increasing, at f_{c3}, impedance of the inductor $L_m/2$ is higher than the noise source impedance $Z_s = f\ (L_s, C_s)$, so that the noise is further blocked by the inductor and thus the filter provides −60 dB/dec attenuation. The resonance at 2.5 MHz is eliminated due to the *LCL* topology. Fang *et al*. [35] provide more discussion on this impedance mismatching and its influences to the filter's in-circuit attenuation. Once knowing the bare noise spectrum and noise load/source impedances, the filter's impedance can be determined, thus can be projected in to the filter's material and geometry.

According to the simulation result in Fig. 20, the in-circuit attenuation of improved design 2 has a resonant peak at low frequency (500 kHz), while the in-circuit attenuation of improved design 1 has resonance at much higher frequency (2.5 MHz). According to the ac resistance shown in Fig. 15, the ac resistance at 2 MHz is six times higher than that at 500 kHz. Therefore, the resonance peak of Improved 1 design can be damped by ac resistance. Because of this benefit, the improved design 1 is selected for the improved busbar filter. Equation (12) shows the derived CM in-circuit attenuation for improved design 1, where $\mathrm{Z_{inductor}}$ is the impedance of the one-turn inductor, l is the total length of ground-connected nickel layers, as shown in Fig. 21. Fig. 21 shows the construction of improved design 1. A high permeability, nanocrystalline, toroid core is used to build the one-turn inductor. Fig. 22 shows the busbar filter with reduced grounding capacitance to meet the safety standards (reduced

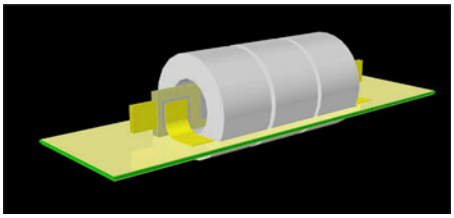

Fig. 23. Improved busbar filter combined with one-turn inductor.

capacitance filter) and Fig. 23 illustrates the improved busbar filter with a one-turn inductor. The geometry selection of the one-turn inductor core is straightforward: the inner diameter of the core should be larger than the width of the busbar filter and the cross-sectional area of the core can be calculated based on the total CM volt–second on the one-turn inductor [28], [30], [31], [41]. The inductor impedance Z_{inductor} can be calculated using (13) where A_L is the core inductance per turn in datasheet, OD is the outer diameter and ID is the inner diameter of the core, and μ_r is the relative permeability of the magnetic material. Equations (10)–(13) link the busbar filter's geometry and material parameters to its in-circuit attenuation, which gives straightforward guidelines for the busbar filter design and implementation in real applications.

High-permeability magnetic core gives high CM inductance, and also increases the Z_{11} and Z_{22} of the busbar filter, as shown in (11). Thus, high-permeability magnetic cores can help to improve the filter attenuation. Regarding the selection of inductor material in this research, high permeability and high flux density is preferred as traditional design, and planar core is also preferred to obtain higher form factor. Higher permeability gives higher inductance and increases the filter's attenuation. The available cores in the market include ferrite cores, amorphous cores, and nanocrystalline cores. Ferrite core has flat frequency response of permeability, and planar ferrite core is available in the market; however, its initial relative permeability (no higher than 10000) and saturation flux density (usually around 0.4 T) are lower than amorphous cores and nanocrystalline cores; amorphous cores and nanocrystalline cores have much higher permeability (>100000) and saturation flux density, and amorphous core/nanocrystalline core usually has higher core loss at higher frequencies. In EMI filtering this characteristic helps to increase filter's attenuation and provide damping at high frequencies. The disadvantage is that amorphous core/nanocrystalline core comes in tape wounded form and hard to make into planar cores. In this research, nanocrystalline toroid core is selected to obtain higher permeability, and just to demonstrate the idea of combining the busbar filter and one-turn inductor. Eddy current loss of the magnetic core is also a part of ac frequency-dependent loss. This eddy current loss provides damping to the filter's high-frequency resonances, and helps to dissipate the high-frequency noise energy.

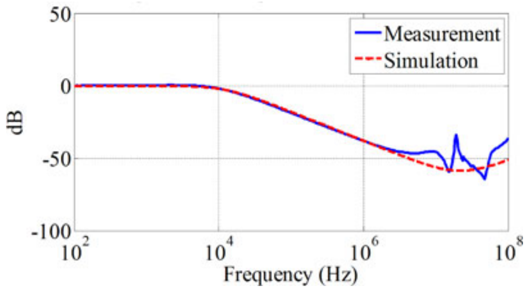

Fig. 24. DM small-signal insertion gain: measurement versus simulation.

From Fig. 17(a), it can be found that

$$V_s = \frac{V_N Z_{\text{LISN}}}{(Z_{\text{LISN}} + Z_s)}.$$

Use Fig. 19 to present the filter topology, and use the length of CM capacitance shown in Fig. 21, the capacitance on each end of the filter can be represented as

$$Z_{Cy1} = Y_0 l_{\text{cap}} k_2/2 \qquad (k_2 = 1).$$

Since the magnetic core is added, the impedance of the one-turn inductor plays major role as a CM inductor. Define // as the parallel of two impedances, it can be found that

$$V_o = \frac{V_N}{(Z_s + Z_{Cy1}//(Z_{\text{inductor}} + Z_{Cy1}//Z_{\text{LISN}}))} \cdot \frac{Z_{Cy1}//(Z_{\text{inductor}} + Z_{Cy1}//Z_{\text{LISN}})}{(Z_{\text{inductor}} + Z_{Cy1}//Z_{\text{LISN}})} \cdot (Z_{Cy1}//Z_{\text{LISN}}).$$

Combine the aforementioned equations, we obtain V_o/V_s, as shown (12) and (13), at the bottom of this page.

V. EXPERIMENTAL RESULTS

To verify the lumped model developed in Section III, small-signal measurement results are compared with SABER circuit simulation results. The equivalent circuits used in SABER simulation are shown in Figs. 11 and 12. With the extracted parameters listed in Tables I and II, the simulated insertion gain using this simplified lumped model matches the experimental result, as shown in Figs. 24 and 25. It can be seen in Figs. 24 and 25 that the model provides satisfactory accuracy up to megahertz range. Above megahertz range, the two results start to deviate. However, the difference between simulation and experiments at high frequency hangs around 10 dB, and this difference can be further eliminated by improving the model's accuracy. This approves that the lumped model provides both simplicity and acceptable accuracy for EMI noise reduction in this case.

$$\frac{V_o}{V_s} = \frac{(Z_{\text{LISN}} + Z_s) Y_0^2 l_{\text{cap}}^2}{(Z_{\text{LISN}} + Z_s + Z_{\text{inductor}}) Y_0^2 l_{\text{cap}}^2 + (4 Z_{\text{LISN}} Z_s + 2 Z_s Z_{\text{inductor}} + 2 Z_{\text{inductor}} Z_{\text{LISN}}) Y_0 l_{cap} + 4 Z_{\text{LISN}} \cdot Z_s \cdot Z_{\text{inductor}}} \qquad (12)$$

$$Z_{\text{inductor}} = 2\pi f \cdot n \cdot A_L = \frac{2\pi f \mu_0 \mu_r A_c}{\pi (OD - ID)} \qquad (13)$$

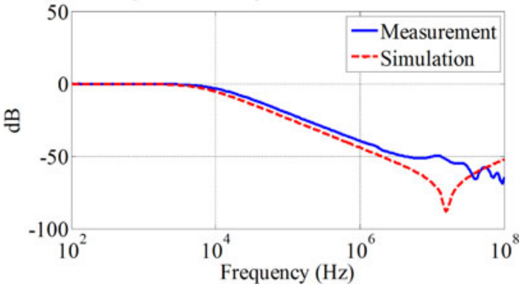

Fig. 25. CM small-signal insertion gain: measurement versus simulation.

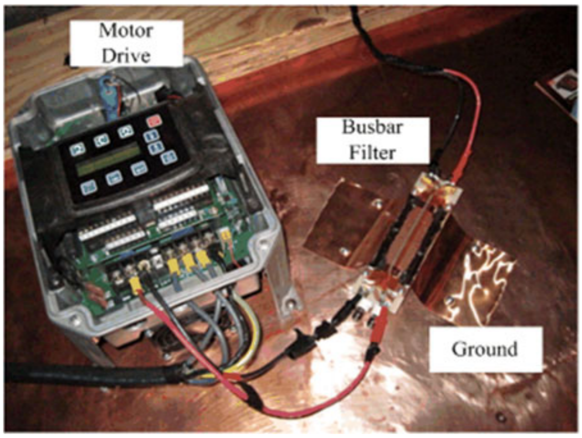

Fig. 26. Busbar filter in a motor drive system.

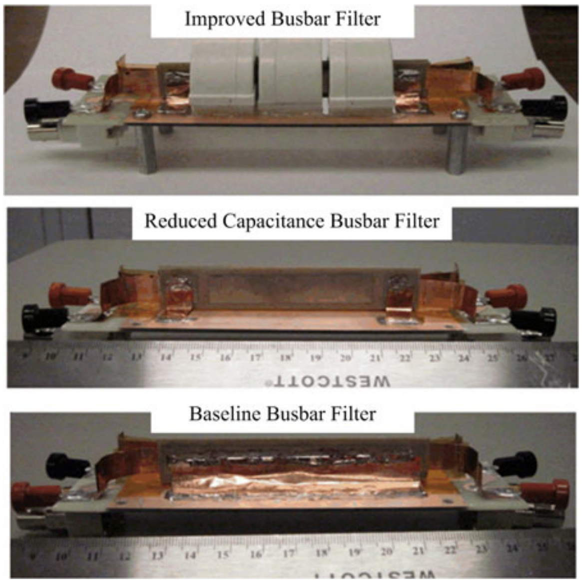

Fig. 27. Different busbar filters.

TABLE III
ELECTRICAL PARAMETERS IN IMPROVED BUSBAR FILTER DESIGN

Parts	Small Signal Value	In-circuit Value
DM capacitance	0.57μF	0.2μF
DM inductance	40nH	40nH
DM resistance	72mΩ	72mΩ
CM capacitance	0.2μF	0.1μF
CM nickel inductance	40nH	40nH
CM One-Turn Inductor	73.2μH@100kHz	
CM resistance	60mΩ	60mΩ

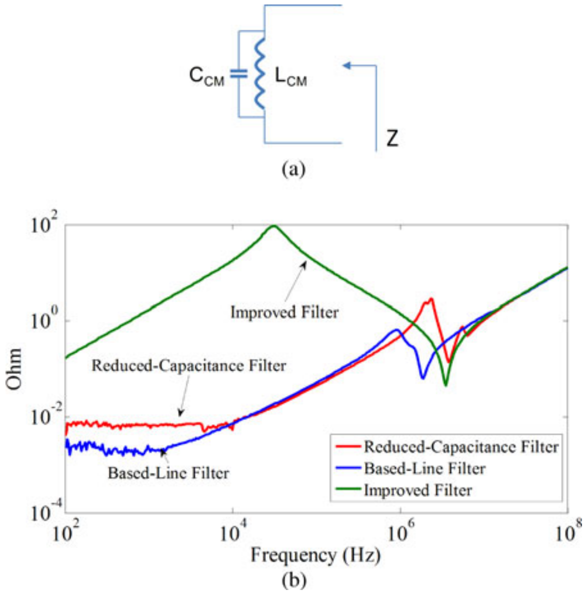

Fig. 28. Short-circuit CM impedance of different versions of busbar filter. (a) First-order equivalent circuit. (b) Measured impedances.

Based on the analyses and simulations presented above, three different busbar filters, as shown in Fig. 27, are fabricated and tested. The busbar filter described in Section II is taken as the "baseline filter," which obtains CM capacitance of 0.5 μF and no magnetic cores. The other two have the limited CM capacitance of 0.1 μF. The one called "reduced capacitance filter" has the same geometry as the baseline filter, but limited capacitance and no magnetic cores. It is an intermediate filter for the comparison to understand how reducing CM capacitance can influence the filter's performance. The one called "improved filter" has the same geometry as the baseline filter, but limited capacitance and also magnetic cores.

Both small-signal and in-circuit tests were conducted. The in-circuit tests are performed with a 2-kW motor drive with 300-V dc-bus voltage. The filters are screwed on the grounded copper plate on the test bench using copper foils as shown in Fig. 26. The parameters of the improved busbar filter are shown in Table III. The magnetic cores used in the prototype are the Finmet toroid core F1AH0700 from METGLAS. Use of toroid core gives flexibility of stacking cores with the same cross section into one core with the designed height to achieve required inductance. These three cores form one big core, and the big core has the designed core height l_{core}, as shown in Fig. 18.

Fig. 28(b) illustrates that the transmission-line busbar filter with additional magnetic cores has a much higher short-circuit CM impedance than the baseline filter. The short-circuit CM impedance is obtained by shorting one end of the CM filter to the

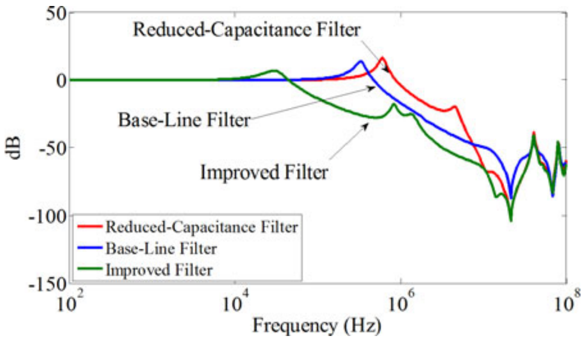

Fig. 29. CM transfer gains of different busbar filters.

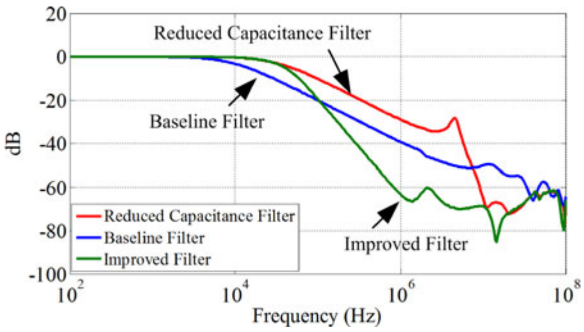

Fig. 30. CM small-signal insertion gains of different busbar filters.

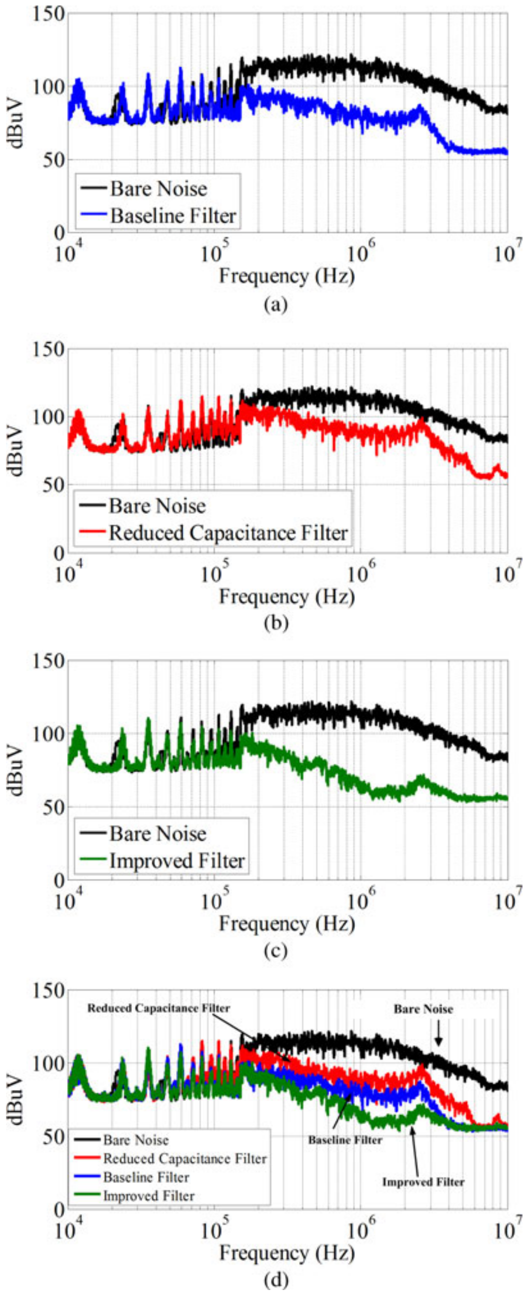

Fig. 31. CM in-circuit noise spectrum measurement in experiments. (a) Bare noise and noise with baseline basbar filter. (b) Bare noise and noise with reduced capacitance filter basbar filter. (c) Bare noise and noise with improved busbar filter. (d) Noise spectrum comparisons using different filters.

ground and measuring the impedance of the other end. Fig. 27(a) shows the first-order equivalent circuit for this impedance measurement. The magnetic core significantly increases the low-frequency impedance by more than 1000 times at 10 kHz. This is contributed by the increased low-frequency inductance. There is an impedance peak around 30 kHz. This is due to the parallel resonance between L and C in Fig. 27(a) (the one-turn CM inductance is around 280 μH at 30 kHz). Figs. 29 and 30 show the small-signal transfer gains and the insertion gains of the filters. In Fig. 29, when the grounding capacitance is reduced to 0.1 μF, the filter's corner frequency increases from 500 kHz up to around 800 kHz; with magnetic cores, the corner frequency then decreases to 40 kHz. Fig. 30 shows the improvement based on small-signal insertion gain test, with load/source impedances equal to 50 Ω. The insertion gain's slope increased from -20 to -40 dB/dec after the magnetic core is added to the busbar filter because an LC filter has $-$ 40 dB/dec rollover slope. On the other hand, before the core is added to the filter, the low-frequency corner frequency of the filter is determined by load resistance R and CM capacitance since the CM inductance is too small to have attenuation at low frequencies. It has only a -20 dB/dec rollover slope. It is also shown that the improved design has a small resonance at around 2 MHz, while the reduced capacitance busbar filter has a higher resonance at 7 MHz. However, they are damped by nickel layer's ac resistance.

The CM in-circuit test results are shown in Fig. 31. Black curves in Fig. 31 illustrate the bare noise (the noise without EMI filters) of the motor drive system. The peak value of the bare noise hits 105 dBμV at 12 kHz, and then it increases by 20 dB/dec. At 150 kHz, the bare noise hits its maximum value 120 dB, and this amplitude stays from 150 kHz to around 1.5 MHz. The amplitude of bare noise spectrum starts decreasing by -40 dB/dec when the frequency goes above 1.5 MHz. The blue curve in Fig. 31(a) shows the noise with the baseline filter (filter grounding capacitance 0.5 μF). Once the baseline busbar filter is installed, the noise starts decreasing from about 70 kHz with a slope of approximately -20 dB/dec. Fig. 31(b) illustrates the in-circuit performance of the reduced capacitance filter (filter grounding capacitance reduces from 0.5 to 0.1 μF). The reduced capacitance filter design has similar attenuation slope as the baseline filter, but its corner frequency moves to higher frequencies. The noise spectrum with reduced capacitance filter starts deviating from the bare noise around 150 kHz, with -20 dB/dec attenuation; the green curve in Fig. 31(c) shows the noise measured with improved busbar filter (filter grounding capacitance reduces from 0.5 to 0.1 μF, magnetic cores are added), and it shows that the improved busbar filter starts attenuating noise from about 60 to 70 kHz with a rate of -40 dB/dec. Fig. 31(d) gives the comparison of the experiment results with all these filters. It can be seen that the reduced capacitance filter almost has the same trend in the attenuation as the baseline filter. The reduced capacitance filter provides less attenuation than the baseline filter due to its limited CM capacitance. Although the improved filter has the same limited capacitance as the reduced capacitance filter, it provides significant attenuation at lower cutoff frequency due to the one-turn inductor structure. Fig. 31(d) also shows that the attenuation slope of the improved filter is almost twice of which provided by the baseline filter. The improved busbar filter shows a substantial improvement on its noise attenuation. The CM noise is extracted using noise separator [23]–[25].

The final test is conducted with full load (7 A). The low-frequency/dc current is carried by the copper layers in the middle, and ceramic is also a good heat conductor. The copper layer cross area is $10\text{ mm} \times 0.15\text{ mm} = 1.5\text{ mm}^2$, and the total resistance of the busbar is 2.2 mΩ. The motor drive is 2 kW with 300-V dc input, the maximum dc input current is 6.7 A, so that the current density is 4 A/mm^2, which is pretty low for busbar design. The total busbar loss is 99 mW, and the surface area for heat dissipation is $10\text{ mm} \times 100\text{ mm} \times 2 = 2000\text{ mm}^2$. In that case, the temperature rise is very low. This can also be verified by the thermal image. Fig. 32 is taken when the filter is operated in system at 7 A for 30 min, the ambient temperature is 22 °C.

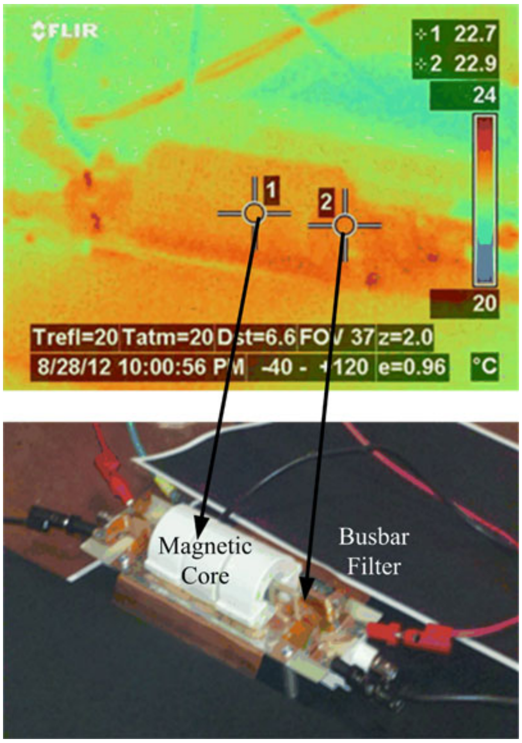

Fig. 32. Thermal image of the improved busbar filter (tested for 30 min with 7-A current).

VI. Discussion and Conclusion

This paper systematically discussed the design, application, and improvement of the transmission-line busbar filters for a motor drive system. The paper starts from the history and motivations of transmission-line busbar filter concepts. It introduces the transmission-line filter's basic principle and its fabrication processes. The paper includes a lot of research efforts from circuit simulations/FEA simulations, small-signal measurement, and in-circuit simulation to model the filter's in-circuit behavior. The MIL-461 standard was selected in this research, which defines the noise limit from 10 kHz to 10 MHz. This research proves that the low-frequency-lumped model and related equations are good enough for the filter design and its in-circuit performance evaluation to some extent, within the test range defined by MIL-461 standard for this motor drive system. Based on the modeling efforts, the paper gives the relationship between the filter geometry and its in-circuit attenuation. This relationship can be used as the filter design guideline.

To improve the performance of the existing transmission-line busbar filters, this paper also systematically and experimentally investigated potential solutions. A hybrid solution of combining a one-turn inductor and the transmission-line busbar filter has been proposed, analyzed, and tested in the research. This solution gives the freedom and simplicity to designers to choose different geometries/materials/additional chokes to achieve the attenuation they want.

The improved busbar filter based on this hybrid solution inherits the benefits from existing transmission-line filters. The manufacturing process of the proposed improved design is compatible with semiconductor process, which gives potential for low-cost large quantity assembly. The improved design is a filter with low profile and small/controllable parasitics. The planar transmission-line busbar is combined with a one-turn inductor, and both of them have negligible EPC due to the long distance between input and output ports. The filter capacitor is integrated by planar ceramic layers, and its ESL is also trivial due to the small length of displacement current paths. Moreover, the improved design provides higher noise attenuation since it combines a one-turn inductor and obtains higher inductance compared with the traditional transmission-line busbar filter design. Adding extra cores to improve the filter's performance increases the filter's volume/weight, if just looking at the filter itself. Nevertheless, the proposed design utilizes the busbar of the converter, which is an existing component in the system, and modifies its structure to contain the EMI noise inside the converter. It can help to reduce or eliminate the discrete filters in the converter system and bring benefits to the power density from the system point of view. This proposed design provides a multifunctional integrated component which performs both as a busbar and an EMI filter. This paper contributes a system approaches for EMI reduction.

The paper includes detail design procedures and models for the transmission-line busbar filter and its improved design. It also compares performances of different busbar filters in simulation and experiments. Analysis and simulation in the paper have been verified by the experiment results. This paper provides an integrated EMI containment solution for medium-power electronics systems.

ACKNOWLEDGMENT

The authors would like to thank Dr. J. D. Van Wyk and Dr. Y. Liang for their help on the research.

REFERENCES

[1] R. M. Cuzner, "Impacts to the power density of ship electric drives," *IEEE Power Electron. Soc. Newslett.*, vol. 16, no. 3, pp. 10–12, 2004.

[2] L. Fang, R. Robutel, W. Shuo, F. Wang, and D. Boroyevich, "Integrated input EMI filter for a 2 kW DC-fed 3-phase motor drive," in *Proc. Appl. Power Electron. Conf. Expo.*, 2009, pp. 325–329.

[3] J. D. Van Wyk, Jr., W. A. Cronje, J. D. van Wyk, C. K. Campbell, and P. J. Wolmarans, "Power electronic interconnects: skin- and proximity-effect-based frequency selective-multipath propagation," *IEEE Trans. Power Electron.*, vol. 20, no. 3, pp. 600–610, May 2005.

[4] P. J. Wolmarans, J. D. van Wyk, J. D. van Wyk, Jr., and C. K. Campbell, "Technology for integrated RF-EMI transmission line filters for integrated power electronic modules," in *Proc. IEEE Ind. Appl. Conf.*, Oct. 2002, vol. 3, pp. 1774–1780.

[5] L. Zhao, R. Chen, and J. D. van Wyk, "An integrated common mode and differential mode transmission line RF-EMI filter," in *Proc. IEEE Power Electron. Spec. Conf.*, Jun. 2004, vol. 6, pp. 4522–4526.

[6] R. Chen, Y. Liang, and J. D. Van Wyk, "Integrated transmission line EMI filter," in *Proc. 4th Int. Conf. Integr. Power Syst.*, 2006, pp. 1–6.

[7] C. K. Campbell, J. D. van Wyk, and P. J. Wolmarans, "Improved transmission-line attenuators for integrated power filters in the RF band," *IEEE Trans. Compon. Packag. Technol.*, vol. 27, no. 2, pp. 311–316, Jun. 2004.

[8] M. C. Smit, J. A. Ferreira, and J. D. Van Wyk, "Application of transmission line principles to high frequency power converters," in *Proc. IEEE Power Electron. Spec. Conf.*, Jun./Jul. 1992, vol. 2, pp. 1423–1430.

[9] L. Zhao and J. D. van Wyk, "Electromagnetic modeling of an integrated RF EMI filter," in *Proc. IEEE Ind. Appl. Conf.*, Oct. 2003, vol. 3, pp. 1601–1607.

[10] A. C. Baisden, D. Boroyevich, and J. D. van Wyk, "Impedance interaction and EMI attenuation in converters with an integrated transmission-line filter," in *Proc. IEEE Appl. Power Electron. Conf.*, Feb./Mar. 2007, pp. 1203–1208.

[11] A. C. Baisden, D. Boroyevich, and J. D. van Wyk, "Enhanced design of an integrated transmission-line bus filter," in *Proc. IEEE Power Electron. Spec. Conf.*, Jun. 2007, pp. 3029–3033.

[12] A. C. Baisden, D. Boroyevich, and J. D. van Wyk, "High frequency modeling of a converter with an RF-EMI filter," in *Proc. IEEE Ind. Appl. Conf.*, Oct. 2006, vol. 5, pp. 2290–2295.

[13] L. Fang, A. C. Baisden, D. Boroyevich, N. Khai, F. Wang, P. Mattavelli, L. Coppola, N. Gazel, and K. Yong, "An improved design for transmission line busbar EMI filter," in *Proc. IEEE Energy Convers. Congr. Expo.*, Sep. 2010, pp. 1232–1238.

[14] Y. Liang, R. Chen, and J. D. van Wyk, "Large signal dielectric characterization for integrated electromagnetic power passives," in *Proc. IEEE Appl. Power Electron. Conf. Expo.*, Mar. 2005, pp. 979–985.

[15] Y. Liang, J. D. van Wyk, and K. Ngo, "Parametric characterization of differential-mode transmission line EMI filter," in *Proc. IEEE Appl. Power Electron. Conf.*, Feb.–Mar. 2007, pp. 1217–1223.

[16] M. Hartmann, H. Ertl, and J. W. Kolar, "EMI filter design for a 1 MHz, 10 kW Three-Phase/Level PWM rectifier," *IEEE Trans. Power Electron.*, vol. 26, no. 4, pp. 1192–1204, Apr. 2011.

[17] X. Wu, D. Xu, Z. Wen, Y. Okuma, and K. Mino, "Design, modeling, and improvement of integrated EMI filter with flexible multilayer foils," *IEEE Trans. Power Electron.*, vol. 26, no. 5, pp. 1344–1354, May 2011.

[18] *Requirements for the Control of Electromagnetic Interference Characteristics of Subsystems and Equipment*, Department of Defense Interference Standard, MIL-STD-461F, Dec. 2007.

[19] S. Xing and Z. Wu, "Characteristic research of bearing currents in inverter-motor drive systems," in *Proc. IEEE Power Electron. Motion Control Conf.*, Aug. 2006, pp. 1–4.

[20] J. M. Erdman, R. J. Kerkman, D. W. Schlegel, and G. L. Skibinski, "Effect of PWM inverters on AC motor bearing currents and shaft voltages," *IEEE Trans. Ind. Appl.*, vol. 32, no. 2, pp. 250–259, Mar./Apr. 1996.

[21] L. Fang, D. Boroyevich, P. Mattavelli, and X. Zhang, "On discussion of switching frequency impacts on DC-fed motor drive EMI filter design," in *Proc. IEEE Appl. Power Electron. Conf. Expo.*, Feb. 2012, pp. 623–627.

[22] L. Fang, Z. Xuning, D. Boroyevich, P. Mattevelli, X. Jing, F. Wang, and N. Gazel, "On discussion of AC and DC side EMI filters design for conducted noise suppression in DC-fed three phase motor drive system," in *Proc. IEEE Appl. Power Electron. Conf. Expo.*, Mar. 2011, pp. 667–672.

[23] S. Wang, F. C. Lee, and W. G. Odendaal, "Characterization, evaluation, and design of noise Separator for conducted EMI noise diagnosis," *IEEE Trans. Power Electron.*, vol. 20, no. 4, pp. 974–982, Jul. 2005.

[24] S. Wang, L. Fang, and F. C. Lee, "Characterization and design of three-phase EMI noise separators for three-phase power electronics systems," *IEEE Trans. Power Electron.*, vol. 26, no. 9, pp. 2426–2438, Sep. 2011.

[25] J. Stahl, D. Kuebrich, A. Bucher, and Duerbaum, "Characterization of a modified LISN for effective separated measurements of common mode and differential mode EMI noise," in *Proc. IEEE Energy Convers. Congr. Expo.*, Sep. 2010, pp. 935–941.

[26] P. C. Magnusson, G. C. Alexander, and V. K. Tripathi, *Transmission Lines and Wave Propagation*, 3rd ed. Boca Raton, FL, USA: CRC Press, 1992.

[27] J. Jiguang, *Circuit Theory (Part II)*. Beijing, China: Tsinghua Univ. Press, 1996.

[28] L. Fang, D. Boroyevich, P. Mattevelli, and N. Gazel, "A comprehensive design for high power density common mode EMI inductor," in *Proc. IEEE Energy Convers. Congr. Expo.*, Sep. 2011, pp. 1861–1867.

[29] J. Dong, L. Rixin, W. Fei, L. Fang, W. Shuo, and D. Boroyevich, "Study of conducted EMI reduction for three-phase active front-end rectifier," *IEEE Trans. Power Electron.*, vol. 26, no. 12, pp. 3823–3831, Dec. 2011.

[30] L. Fang, W. Shuo, F. Wang, D. Boroyevich, N. Gazel, and K. Yong, "Common mode voltage in DC-fed motor drive system and its impact on the EMI filter," in *Proc. IEEE Appl. Power Electron. Conf. Expo.*, Feb. 2010, pp. 1272–1278.

[31] L. Fang, W. Shuo, W. Fei, D. Boroyevich, N. Gazel, K. Yong, and A. C. Baisden, "Analysis of CM volt-second influence on CM inductor saturation and design for input EMI filters in three-phase DC-fed motor drive systems," *IEEE Trans. Power Electron.*, vol. 25, no. 7, pp. 1905–1914, Jul. 2010.

[32] A. M. Hava and E. Un, "Performance analysis of reduced common-mode voltage PWM methods and comparison with standard PWM methods for three-phase voltage-source inverters," *IEEE Trans. Power Electron.*, vol. 24, no. 1, pp. 241–252, Jan. 2009.

[33] L. Ran, S. Gokani, J. Clare, K. J. Bradley, and C. Christopoulos, "Conducted electromagnetic emissions in induction motor drive systems. II. Frequency domain models," *IEEE Trans. Power Electron.*, vol. 13, no. 4, pp. 768–776, Jul. 1998.

[34] H. Akagi and T. Oe, "A specific filter for eliminating high-frequency leakage current from the grounded heat sink in a motor drive with an active front end," *IEEE Trans. Power Electron.*, vol. 23, no. 2, pp. 763–770, Mar. 2008.

[35] L. Fang, D. Boroyevich, and P. Mattavelli, "Improving EMI filter design with in circuit impedance mismatching," in *Proc. IEEE Appl. Power Electron. Conf. Expo.*, Feb. 2012, pp. 1652–1658.

[36] Z. Xuning, L. Fang, D. Dong, P. Mattavelli, and D. Boroyevich, "CM noise containment in a DC-fed motor drive system using DM filter," in *Proc. IEEE Appl. Power Electron. Conf. Expo.*, Feb. 2012, pp. 1808–1813.

[37] L. W. Li, M. S. Leong, P. S. Kooi, and T. S. Yeo, "Mutual impedance of two probes located in two different waveguide regions separated by a homogeneous dielectric slab: Fullwave analysis," IEE Proc. Microw., Antennas Propag., vol. 144, no. 5, pp. 329–336, Oct. 1997.

[38] L. Qian, S. Wang, A. C. Baisden, F. Wang, and D. Boroyevich, "EMI suppression in voltage source converters by utilizing dc-link decoupling capacitors," *IEEE Trans. Power Electron.*, vol. 22, no. 4, pp. 1417–1428, Jul. 2007.

[39] L. Xing and J. Sun, "Conducted common-mode EMI reduction by impedance balancing," *IEEE Trans. Power Electron.*, vol. 27, no. 3, pp. 1084–1089, Mar. 2012.

[40] S. Wang, Y. Y. Maillet, F. Wang, R. Lai, F. Luo, and D. Boroyevich, “Parasitic effects of grounding paths on common-mode EMI filter’s performance in power electronics systems,” *IEEE Trans. Ind. Electron.*, vol. 57, no. 9, pp. 3050–3059, Sep. 2010.

[41] A. Virtanen, “Comparison of common-mode voltages in frequency converters with alternative space vector modulation methods,” in *Proc. IEEE Power Electron. Spec. Conf.*, Jun. 2008, pp. 2248–2256.

Fang Luo (S’06–M’10) received the B.S. degree in electrical engineering and the Ph.D. degree from Huazhong University of Science and Technology, Wuhan, China, in 2003 and 2010, respectively. Since 2007, he has been working toward the Ph.D. degree with the Center for Power Electronics Systems (CPES), Virginia Tech, Blacksburg, VA, USA, supported by the Chinese Scholarship Council and CPES.

From 2010 to 2012, he was a Postdoctoral Researcher at CPES, Virginia Tech, where he is currently a Senior Research Associate. His research interests include high-density electromagnetic interference filtering solution and power module packaging for wide band-gap devices.

Andrew Carson Baisden received the B.S. degree in electrical engineering from the Illinois Institute of Technology, Chicago, IL, USA, in 2003, the second B.S. degree in mathematics from Benedictine University, Lisle, IL, USA, in 2003, and the M.S. and Ph.D. degrees in electrical engineering from the Center for Power Electronics Systems (CPES), Virginia Polytechnic Institute and State University, Blacksburg, VA, USA, in 2006 and 2009, respectively.

From 2000 to 2002, he was with Argonne National Laboratories as a Research Lab Assistant. In 2006, he was a Power Electronics Development Engineer for Rockwell Automation. From 2003 to 2009, he was with CPES as a Graduate Research Assistant. He then joined the Applied Physics Laboratory, Johns Hopkins University, as a Power Electronics Engineer for space applications. His research interests include power conversion systems and analog design, electromagnetic interference/electromagnetic compatibility, electronics packaging, and integrated power electronic systems.

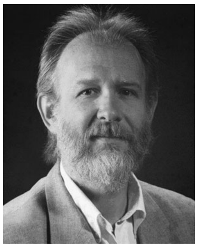

Dushan Boroyevich (S’81–M’86–SM’03–F’06) received the Dipl.Ing. degree from the University of Belgrade, Belgrade, Serbia, in 1976, the M.S. degree from the University of Novi Sad, Novi Sad, Serbia, in 1982, and the Ph.D. degree from Virginia Polytechnic Institute and State University (Virginia Tech), Blacksburg, VA, USA, in 1986.

From 1986 to 1990, he was an Assistant Professor and the Director of the Power and Industrial Electronics Research Program at the Institute for Power and Electronic Engineering, University of Novi Sad, where he later became the Head of the Institute. He then joined the Bradley Department of Electrical and Computer Engineering, Virginia Tech, as an Associate Professor, where he is currently the American Electric Power Professor and the Co-Director of the Center for Power Electronics Systems. His research interests include multiphase power conversion, electronic power distribution systems, power electronics systems modeling and control, and multidisciplinary design optimization.

Dr. Boroyevich received the IEEE William E. Newell Power Electronics Technical Field Award. From 2011 to 2012, he was the President of the IEEE Power Electronics Society.

Khai D. T. Ngo (S’82–M’84–SM’02) received the B.S. degree from California State Polytechnic University, Pomona, CA, USA, in 1979, and the M.S. and Ph.D. degrees from the California Institute of Technology, Pasadena, CA, USA, in 1980 and 1984, respectively, all in electrical and electronics engineering.

He is currently a Professor of electrical and computer engineering at Virginia Polytechnic Institute and State University (Virginia Tech). From 1984 to 1988, he was a member of Technical Staff at General Electric Corporate Research and Development Center, Schenectady, NY, USA. Between 1988 and 2006, he was with the University of Florida, Gainesville, FL, USA. At Virginia Tech, he pursues technologies for integration and packaging of power passive and active components to realize building blocks for power electronic systems. These technologies lead to power conversion systems with higher efficiency and higher power density. He also focuses on topologies, control, emission, and integration issues for RF power converters. Other research interests include magnetic materials and components, energy reclamation, and power integrated circuits.

Shuo Wang (S’03–M’06–SM’07) received the Ph.D. degree from Virginia Polytechnic Institute and State University (Virginia Tech), Blacksburg, VA, USA, in 2005.

Since 2010, he has been a faculty member in the Department of Electrical and Computer Engineering, University of Texas at San Antonio (UTSA). Before joining UTSA, he was with electrical power systems, General Electric (GE) Aviation Systems, West Chester, OH. Before joining GE, he was a Research Assistant Professor at Virginia Tech. He has published more than 90 IEEE journal and conference papers. He holds six U.S. patents and has one more pending.

Dr. Wang received the Best Transaction Paper Award from the IEEE TRANSACTIONS ON POWER ELECTRONICS in 2006, and two William M. Portnoy Awards from the IEEE Industry Applications Society in 2004 and 2012, respectively. He is an Associate Editor for the IEEE TRANSACTIONS ON INDUSTRY APPLICATIONS. In March 2012, he received the prestigious National Science Foundation CAREER Award (Faculty Early Career Development Award).

Paolo Mattavelli (S’95–A’96–M’00–SM’10) graduated (with honors) received the Ph.D. degree in electrical engineering from the University of Padova, Padova, Italy, in 1995.

From 1995 to 2001, he was a Researcher at the University of Padova. From 2001 to 2005, he was an Associate Professor at the University of Udine, where he led the Power Electronics Laboratory. In 2005, he joined the University of Padova, Vicenza, with the same duties. From 2010 to 2012, he was a Professor and member of the Center for Power Electronics Systems (CPES), Virginia Tech. Since 2013, he has been with the University of Padova, while keeping an adjunct position at Virginia Tech. His main research interests include analysis, modeling and analog and digital control of power converters, grid-connected converters for renewable energy systems and micro-grids, high-temperature and high power density power electronics. In these research fields, he has been leading several industrial and government projects.

From 2003 to 2012, he was an Associate Editor for the IEEE TRANSACTIONS ON POWER ELECTRONICS. From 2005 to 2010, he was the Industrial Power Converter Committee Technical Review Chair for the IEEE TRANSACTIONS ON INDUSTRY APPLICATIONS. During 2003–2006 and 2006–2009, he was also a member at large of the IEEE Power Electronics Society’s Administrative Committee. He received the Prize Paper Award in the IEEE Transactions on Power Electronics in 2005, 2006, and 2011, respectively. He also received the second Prize Paper Award at the IEEE Industry Application Annual Meeting in 2007.